Am J Cancer Res 2019;9(7):1454-1468
www.ajcr.us /ISSN:2156-6976/ajcr0097543

Original Article

Dual-labeled pertuzumab for multimodality image-guided ovarian tumor resection

Hye Jin Lee[1], Emily B Ehlerding[2], Dawei Jiang[3,4], Todd E Barnhart[2], Tianye Cao[3], Weijun Wei[3], Carolina A Ferreira[5], Peng Huang[4], Jonathan W Engle[2], Weibo Cai[1,2,3,5,6]

Departments of [1]Pharmaceutical Sciences, [2]Medical Physics, [3]Radiology, University of Wisconsin-Madison, Madison, WI 53705, USA; [4]Guangdong Key Laboratory for Biomedical Measurements and Ultrasound Imaging, Carson International Cancer Center, Laboratory of Evolutionary Theranostics, School of Biomedical Engineering, Health Science Center, Shenzhen University, Shenzhen 518060, China; [5]Department of Biomedical Engineering, University of Wisconsin-Madison, Madison, WI 53706, USA; [6]University of Wisconsin Carbone Cancer Center, Madison, WI 53705, USA

Received May 26, 2019; Accepted June 14, 2019; Epub July 1, 2019; Published July 15, 2019

Abstract: Pertuzumab is clinically employed in the treatment of cancers over-expressing human epidermal growth factor receptor 2 (HER2). Herein, we developed dual-labeled pertuzumab with a radionuclide (^{89}Zr) and a near-infrared fluorophore (IRDye 800CW) to investigate the feasibility of utilizing dual-labeled monoclonal antibodies (mAbs) with numerous imaging modalities for preoperative imaging and image-guided surgery in ovarian cancer models. MAbs were dually-labeled with ^{89}Zr and IRDye 800CW to generate ^{89}Zr-Df-pertuzumab-800CW or ^{89}Zr-Df-IgG-800CW. Serial positron emission tomography (PET) and near-infrared fluorescence (NIRF) images were acquired up to 72 hours after injection of dual-labeled mAbs to map the tracers' biodistributions. After the last time point, image-guided tumor resection was executed using different modalities (NIRF, Cerenkov luminescence [CL], and β particle imaging) and *ex vivo* studies including biodistribution assays and histology analysis were performed to confirm the *in vivo* imaging data. SKOV3 ovarian cancer cells showed high expression of HER2 and pertuzumab conjugated with Df and IRDye 800CW maintained its binding affinity for these cells. For PET imaging in subcutaneous xenograft ovarian cancer models, ^{89}Zr-Df-pertuzumab-800CW showed a significantly higher tumor-to-muscle ratio compared to the nonspecific ^{89}Zr-Df-IgG-800CW from 24 hours after injection through the last time point (72 h: 30.7 ± 7.4 vs. 7.5 ± 1.8, $P < 0.01$, $n = 3$-4). During image-guided surgery, three imaging modalities including NIRF, CL, and β particle imaging could detect ovarian cancer in both subcutaneous and orthotopic models and each exhibited its own imaging characteristics. In addition, *ex vivo* imaging and biodistribution studies as well as histology analysis corroborated the *in vivo* imaging results. Therefore, we concluded that this single radiolabeled tracer can provide all-in-one contrast for multiple imaging modalities. The dual-labeled mAbs may hold promise to be employed for image-guided tumor surgery as well as diagnosis and staging through balancing out the strengths and weaknesses of various modalities such as PET/CT, NIRF, CL, and β particle imaging.

Keywords: Human epidermal growth factor receptor 2 (HER2), image-guided surgery, near-infrared fluorescence (NIRF) imaging, ovarian cancer, pertuzumab, positron emission tomography (PET), ^{89}Zr

Introduction

Ovarian cancer is an often-fatal gynecologic disease, ranking at fifth among cancer-related deaths for women [1]. According to a recent report, there will be approximately 22,530 of new cases of ovarian cancer in the United States in 2019, and the estimated number of deaths from ovarian cancer will be 13,980 in the same year [2]. Ovarian cancer can be difficult to recognize because clinical signs and symptoms of ovarian cancer are unclear and non-specific (e.g. abdominal bloating, changes in appetite, and urinary discomfort, etc) [3]. Cancer antigen 125 (CA125) has been used as one of the earliest biomarkers for screening ovarian cancer, but it was discovered that the sensitivity of CA125 is low at early stages and its level can also be increased in various physiological conditions [4]. Besides, ovarian cancer

can be developed in any woman even without having high risk factors [3]. For these reasons, many patients who are newly diagnosed already show metastasis in the peritoneal space or outside of the pelvic region [5].

As ovarian cancer spreads mainly through the abdominal cavity [5], complete removal of residual tumor and the minimal safety surgical margin is critical. The standard treatment for advanced ovarian cancer is to remove discernible and palpable tumor tissues and to administer chemotherapy following surgery [6]. However, palpation or visual inspection for removal of tumor burden is not perfect and is subject to the experience of the surgeon. Ataseven et al. confirmed that residual disease following debulking surgery is associated with prognosis in patients with ovarian cancer diagnosed at FIGO (Federation of Gynecology and Obstetrics) stage IV, and complete tumor removal results in the greatest surgical benefits [7]. In this regard, intraoperative image-guided surgery may hold great promise for more accurate and sensitive removal of tumor tissue and potential enhancement of survival rates in patients with ovarian cancer.

To help with this pressing problem, molecular imaging can play a crucial role not only in diagnosis of ovarian cancer but also in staging and treatment. Anatomical imaging can be performed with the help of computed tomography (CT), magnetic resonance imaging (MRI), and ultrasonography. On the other hand, radionuclide-based imaging such as positron emission tomography (PET) or single-photon emission computed tomography (SPECT) can provide biological information with high sensitivity on the molecular level. In clinic, ^{18}F-Fludeoxyglucose [8], which exploits glucose metabolism, or ^{18}F-Fluorothymidine [9], which targets proliferating cells, are widely used for cancer imaging. However, these molecular probes remain suboptimal because they are not highly selective for cancerous cells, and the results can be impacted by the physiological conditions of the patients [8]. In this sense, molecular probes targeting specific markers of diseases can complement the information we get from non-specific probes and may provide additional useful information on abnormal lesions.

Optical imaging based on fluorescence is one of the widely-used methods for image-guided surgery and recently has also been employed in clinical trials [10]. Fluorescence imaging has advantages over PET/CT imaging since it is relatively inexpensive and allows real-time high-resolution imaging without using ionizing radiation [11]. In particular, near-infrared (NIR) fluorophores such as indocyanine green or IRDye 800CW absorb light with wavelengths between 650-900 nm and show low nonspecific autofluorescence from the surrounding target tissues and higher signal-to-background ratios due to better tissue penetration than other fluorophores [10]. However, limitations of fluorescence imaging still remain due to low tissue penetration compared to PET imaging [12]. Furthermore, most of the fluorescent agents available in clinic are non-targeted and therefore non-specific for cancerous tissues, such that there is still a great need for scientific development in this area [10].

Another emerging method that can be used for image-guided surgery is Cerenkov luminescence (CL) imaging. CL imaging can detect the Cerenkov photons which are emitted when charged particles (such as positrons or electrons) travel through dielectric media with speeds faster than that of light in the particular medium [13]. Therefore, one of the advantages of CL imaging is that clinically-used radioisotopes, such as ^{90}Y, ^{68}Ga, and ^{89}Zr, for nuclear imaging or therapy can also be used for CL imaging [13]. In addition, various hand-held devices have been developed that may detect charged particles for intraoperative imaging when equipped with electron-multiplying charge-coupled devices [13]. Therefore, in spite of the radiation exposure for patients and surgeons, CL imaging serves as a companion imaging modality to nuclear imaging and presents an alternative to fluorescence imaging for real-time monitoring during surgery.

Pertuzumab (Perjeta), approved by the United States Food and Drug Administration for breast cancer treatment, interferes with the dimerization of human epidermal growth factor receptor 2 (HER2) with other epidermal growth factor receptors and reduces intracellular signaling pathways [14]. Recently, radiolabeled pertuzumab has also been used for imaging of other cancers such as ovarian cancers in preclinical studies [15, 16]. Expanding upon previous works, in this study, pertuzumab dual-labeled

with ^{89}Zr and IRDye 800CW (^{89}Zr-Df-pertuzumab-800CW) were employed for image-guided ovarian tumor resection following serial PET and NIRF imaging. ^{89}Zr ($t_{1/2}$: 78.4 h; E_{mean} = 0.396 MeV) allowed for sensitive detection of gross tumors through preoperative PET/CT in both subcutaneous and orthotopic models, while IRDye 800CW enabled nearly real-time visualization for surgical ovarian tumor removal through NIRF. Furthermore, CL and β particle imaging played supportive roles during surgery in addition to NIRF imaging, making the developed monoclonal antibody (mAb) tracer useful for image-guided tumor resection in a multimodal setting. Therefore, through modification of the mAbs with radionuclides and near-infrared fluorophores in this study, dual-labeled pertuzumab enabled the use of many imaging techniques, each of which may complement the merits and augment the vulnerabilities of the others.

Material and methods

Cell culture and animal models

Three human ovarian adenocarcinoma cell lines, SKOV3, Caov3, and OVCAR3, were obtained from the American Type Culture Collection (Manassas, VA, USA). Cells were cultured in Dulbecco's Modified Eagle's Medium (DMEM; Gibco) or in RPMI 1640 medium (Gibco), supplemented with 10% fetal bovine serum (Atlanta Biologicals, GA, USA), penicillin (100 U/mL; Gibco), and streptomycin (100 μg/mL; Gibco) at 37°C with 5% CO_2.

All animal experiments were implemented under a protocol approved by the University of Wisconsin Institutional Animal Care and Use Committee. For subcutaneous xenografts, 1 × 10^6 tumor cells (SKOV3) were mixed with Matrigel (BD Biosciences, CA, USA) at ratio of 1:1, and 100 μl of the mixture was subcutaneously implanted in the lower right flank of 6-8-week-old female athymic nude mice (Envigo; *n* = 3-4). Animals were used for experiments when the diameter of their tumors reached 5-10 mm. For orthotopic tumor models, surgical procedures were carried out similarly to those previously reported [15]. To monitor the development of orthotopic tumors, ultrasound imaging (Vevo 2100; FUJIFILM VisualSonics, Toronto, Canada) was performed at 3-4 weeks after implantation. A linear array transducer (MS-400) with 40-MHz center frequency was used to obtain two-dimensional images of mouse ovaries.

Flow cytometry

Cells were harvested and suspended in cold flow cytometry staining buffer (eBioscience; Thermo Fisher Scientific) at a concentration of ~1 × 10^6 cells/mL. After incubation with pertuzumab or Df-pertuzumab-800CW at a concentration of 25 μg/mL in flow cytometry staining buffer on ice for 30-45 min, cells were washed three times with cold PBS, and incubated with Alexa Fluor 488 IgG goat-anti human antibodies (Invitrogen) on ice for 30-45 min. The samples were analyzed using the MACSQuant cytometer (Miltenyi Biotec, Bergisch Gladbach, Germany), and the results were processed using FlowJo software (TreeStar, Ashland, OR, USA).

Internalization assay

For the internalization assay, ~5 × 10^4 SKOV3 cells were seeded into each well of 24-well culture plates and incubated in DMEM supplemented with 10% fetal bovine serum and antibiotics (100 U/mL of penicillin, 100 ug/mL of streptomycin). Cells were allowed to sit overnight under standard cell culture conditions and then treated with 18.5 kBq (~0.1 μg) of ^{89}Zr-Df-pertuzumab-800CW in each well. After 30 min, 2 h, 6 h, or 24 h of incubation, an acid wash was performed with 0.2 M sodium acetate for 1-2 min to collect membrane-bound ^{89}Zr-Df-pertuzumab-800CW and followed by trypsinization to obtain internalized dual-labeled mAbs. Collected fractions were measured in a gamma counter. The fraction of membrane-bound or internalized activity (either membrane-bound or internalized activity/(membrane-bound + internalized activity) was plotted against incubation time.

Dual-labeling of monoclonal antibody

Deferoxamine (Df) and IRDye 800CW were conjugated to mAbs as previously reported [17]. Briefly, pertuzumab (Genentech, San Francisco, CA, USA) was mixed with *p*-SCN-Bn-Df (Macrocyclics, Inc., Dallas, TX, USA) dissolved in DMSO at a mAb:chelator molar ratio of ~1:3 and incubated at room temperature for 2 hours at pH 8.5-9.0. After conjugation, samples were puri-

fied with PD-10 desalting columns (GE Healthcare, Chicago, IL, USA) eluted with 1 × PBS. Then, purified Df-pertuzumab was mixed with IRDye 800CW-NHS-ester at a mAb:dye molar ratio of ~1:2.4 for 2 hours at room temperature and pH 8.0-8.5. The mixture was purified using PD-10 columns. Human serum IgG (a non-specific isotype control) was also conjugated with both Df and IRDye 800CW using similar methods. ^{89}Zr was produced by a PETtrace cyclotron (GE Healthcare) via the ^{89}Y (p, n) ^{89}Zr reaction. For ^{89}Zr radiolabeling, ^{89}Zr (~37 MBq) was diluted into 0.5 M HEPES butter (pH 7.0). Df-pertuzumab-800CW or Df-IgG-800CW was added to the diluted solution at a ratio of 150 μg per 37 MBq at 37°C for 1 hour, and purified using a PD-10 column. The number of chelators per antibody was determined by the isotope dilution method reported previously [18]. The amount of IRDye 800CW per antibody was detected by UV measurement at 780 nm.

Serial PET/CT and fluorescence imaging

Longitudinal PET imaging was performed using an Inveon microPET/microCT scanner (Siemens Medical Solutions, Erlangen, Germany). Both subcutaneous and orthotopic tumor-bearing mice (n = 3-5) were intravenously injected with ^{89}Zr-Df-pertuzumab-800CW or ^{89}Zr-Df-IgG-800CW (1.6-8.4 MBq, 13-38 μg per mouse) and scanned at 2, 6, 24, 48 and 72 h after injection. Region-of-interest analysis was performed and decay-corrected whole-body images were reconstructed using vendor software (Inveon Research Workplace). Tissue uptake was represented as mean percent injected dose per gram of tissue ± standard deviation (mean %ID/g ± SD).

Near infrared fluorescence (NIRF) images were acquired ($\lambda_{ex/em}$: 745/800 nm) immediately following each PET scan using the IVIS Spectrum Imaging System (PerkinElmer, Waltham, MA, USA). For image processing and analysis, vendor software (Living Image) was employed.

Image-guided tumor resection

After the last imaging time point, tumor-bearing mice were euthanized by CO_2 asphyxiation. Tumor tissues were removed based on the multimodality images obtained from preoperative and intraoperative imaging. After the tumor tissues were removed, surgical sites and the excised tumor tissues were detected with the same modalities to confirm the complete removal of all tumor tissues (**Figure 4A**).

For fluorescence ($\lambda_{ex/em}$: 745/800 nm) and CL ($\lambda_{ex/em}$: closed/open) imaging, the IVIS Spectrum Imaging System (PerkinElmer) was used. For Fluobeam (Fluoptics, Grenoble, France) imaging, images were taken at a rate of 2 pictures/sec.

To detect emitted β particles, the Hand-Held RadioLuminescence Imaging (HARLI; Lightpoint Medical, MA, USA) system was used. The HARLI system employs a Peltier-cooled electron-multiplying charge-coupled camera (-80°C) to detect charged particles after their interaction with a CsI scintillating film. The exposure time for each image from the HARLI system was 30 seconds and the field-of-view was 2.17 × 2.17 cm^2. The vendor software, Andor Solis, was employed for the analysis of data and the scale bar was represented in terms of counts.

Ex vivo imaging and biodistribution studies

Ex vivo imaging of major organs and tissues was performed using PET, NIRF and CL imaging. Following the imaging studies, the organs/tissues were wet weighed and counted using an automated gamma counter. Tracer accumulation was represented as %ID/g (mean ± SD). Normal ovary and tumor tissues were embedded in the paraffin for further hematoxylin and eosin staining.

Immunofluorescence staining

Frozen tissue slices of 7-μm thickness were fixed with 4% paraformaldehyde. To prevent non-specific binding of mAbs, tissue slices were blocked with 5% donkey serum for 1 hour at room temperature and followed by incubation with a mixture of pertuzumab (20 μg/ml) and rat anti-mouse CD31 antibody (BD Biosciences; 2 μg/ml) overnight at 4°C. Next, a mixture of Alexa Fluor 488 goat anti-human (5 μg/ml) and Cy3 donkey anti-rat (Thermo Fisher Scientific; 10 μg/ml) secondary antibodies was incubated with the slices. After DAPI mounting, tissue sections were imaged with a Nikon A1R confocal microscope.

Statistical analysis

Quantitative data is expressed as mean ± SD. The quantitative results were analyzed using a

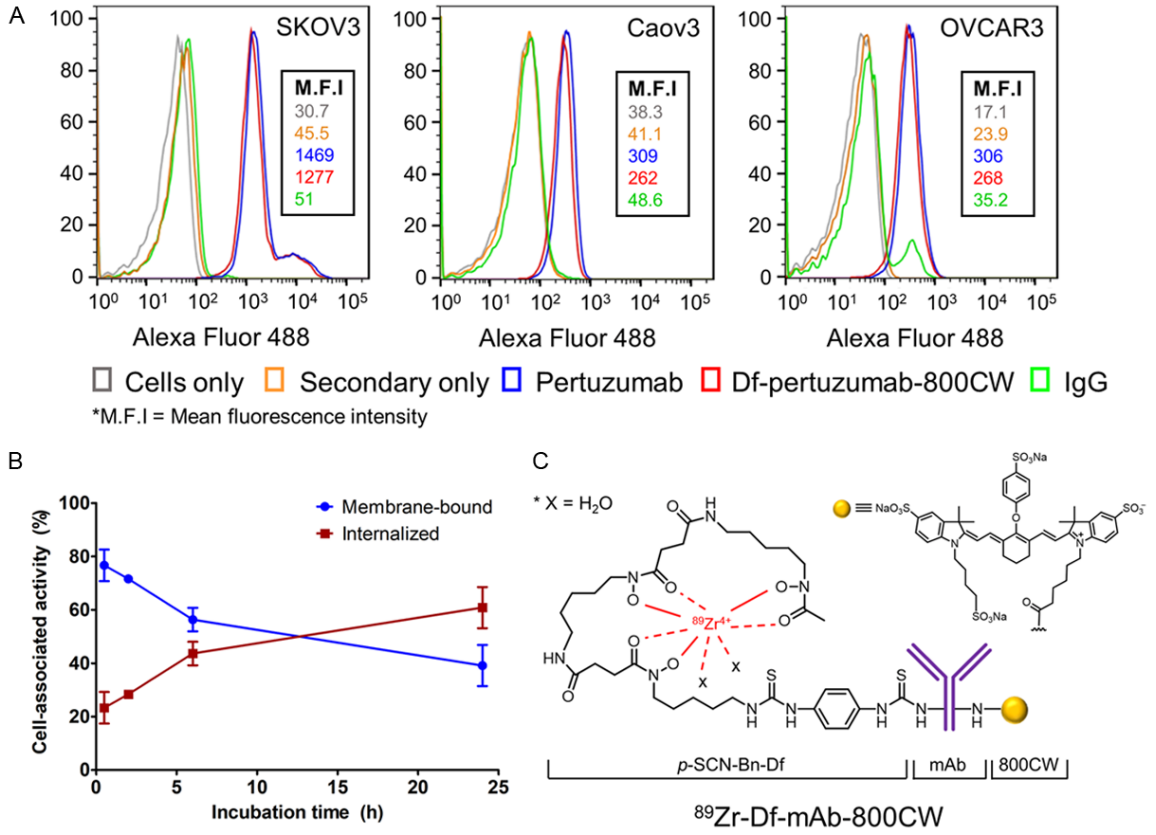

Figure 1. *In vitro* characterization and generation of monoclonal antibodies (mAbs) conjugated with ^{89}Zr and IRDye 800CW. (A) Flow cytometry results showing high HER2 expression on SKOV3 cells compared to Caov3 or OVCAR3. (B) Internalization profile of ^{89}Zr-Df-pertuzumab-800CW in SKOV3 cells. Cell-associated activity (%) was calculated as the radioactivity in the bound or internalized fractions over the total radioactivity associated to cells, n = 3. (C) ^{89}Zr-Df-mAb-800CW was prepared as reported previously [17]. Pertuzumab and a non-specific IgG were employed as the mAbs in this study.

two-tailed unpaired Students' t-test. *P*-values less than 0.05 were considered significant.

Results

In vitro characterization

The expression level of HER2 in different ovarian cancer cells and the immunoreactivities of the mAbs were evaluated through flow cytometry (**Figure 1A**). SKOV3 cells showed high expression of HER2 compared to the two other cell lines, OVCAR3 and Caov3. In addition, there was no significant difference in binding affinity between unconjugated pertuzumab and Df-pertuzumab-800CW in any of the three ovarian cell lines, indicating that conjugation of Df and IRDye 800CW did not compromise the binding affinity of pertuzumab. Therefore, further *in vivo* and *ex vivo* assays with dual-labeled mAbs were performed in the HER2-expressing SKOV3 cell line. The internalization assay showed that ^{89}Zr-Df-pertuzumab-800CW presented high internalization kinetics in SKOV3 cell lines during 24 h (**Figure 1B**). Of all cell-associated mAbs (17.3 ± 3.1% of total incubated activity), 60.8 ± 6.3% were internalized, with a smaller amount remaining on the surface of the cells (39.2 ± 6.3%; n = 3) at 24 h after incubation.

Df/IRDye 800CW conjugation and ^{89}Zr labeling

Based on the isotopic dilution experiment, the average number of chelators per antibody in this study was ~2.3. In addition, UV measurement indicated that the ratio of mAbs to IRDye 800CW was ~1:0.7. This ratio is desirable because antibodies conjugated with less than 1 equivalent mole of fluorophore have little

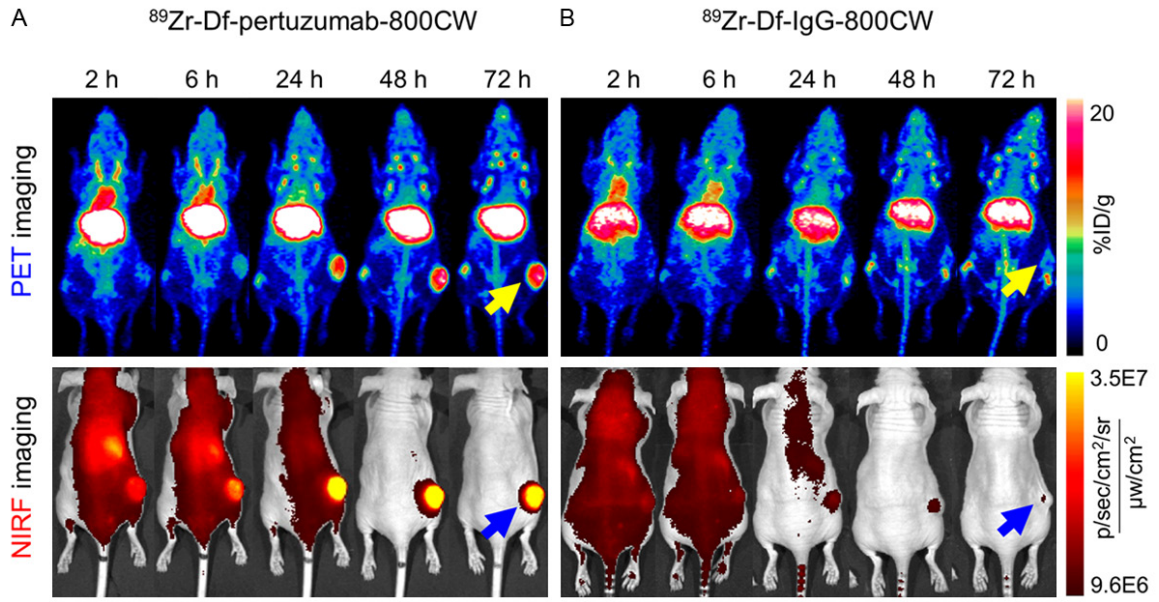

Figure 2. Serial PET and NIRF images of subcutaneous SKOV3 tumor-bearing mice after intravenous injection of the radiolabeled probes. (A) ^{89}Zr-Df-pertuzumab-800CW clearly visualized tumors compared to (B) ^{89}Zr-Df-IgG-800CW as early as 24 h p.i. in both PET and NIRF imaging. For PET imaging, the images are presented as maximum intensity projections (MIPs). The yellow and blue arrows indicate the tumors detected by PET and NIRF imaging, respectively (n = 3-4).

chance of losing of fluorescence signal from self-quenching of dye, which can occur via Förster resonance energy transfer [17]. The mAbs conjugated with Df and IRDye 800CW were then radiolabeled with ^{89}Zr (**Figure 1C**). The radiolabeling yield of the dual-labeled pertuzumab and non-specific IgG with ^{89}Zr was ~70% and ~50% (non-decay corrected), respectively.

Serial PET/NIRF imaging and image-guided tumor resection in subcutaneous tumor models

Time points of 2, 6, 24, 48 and 72 h post-injection (p.i.) were selected for *in vivo* serial PET imaging of subcutaneous SKOV3 tumor-bearing mice. Subcutaneous models were used as a proof-of-concept imaging study since this model is relatively easy to establish and monitor. Imaging results are presented as maximum intensity projections (MIPs) (**Figure 2**). The tumor accumulation of ^{89}Zr-Df-pertuzumab-800CW increased until 48 h and remained steady at 72 h. The uptake of ^{89}Zr-Df-pertuzumab-800CW in the heart/blood was highest at 2 h (12.7 ± 3.5 %ID/g, n = 4) and continuously decreased until the last time point (**Figure 3A**). After 72 h, the tumor/muscle ratio in the ^{89}Zr-Df-pertuzumab-800CW group was significantly higher than that of the ^{89}Zr-Df-IgG-800CW group (30.7 ± 7.4 vs. 7.5 ± 1.8, P < 0.01, n = 3-4; **Figure 3C**).

NIRF imaging was executed at the same time points as PET imaging. At 24 h p.i. of ^{89}Zr-Df-pertuzumab-800CW, the subcutaneous SKOV3 tumor was clearly outlined through fluorescence imaging (**Figure 2A**). Since both PET and NIRF imaging could delineate the tumor in an obvious manner at 72 h p.i., and a significant difference in accumulation was noted between the ^{89}Zr-Df-pertuzumab-800CW and ^{89}Zr-Df-IgG-800CW groups in the PET imaging, image-guided tumor resection was performed at this time point.

Surgical removal of subcutaneous tumors was performed immediately following the last time point of serial PET/NIRF imaging. First, preoperative images of tumor-bearing mice were obtained using multimodality imaging (**Figure 4**). In addition to PET and NIRF imaging (**Figure 2**), CL and β particle imaging could also delineate subcutaneous tumors in a supportive manner (**Figure 4C** and **4D**). During surgery, tumors were removed based on both the preoperative images and the images acquired from intraoperative imaging. In particular, the

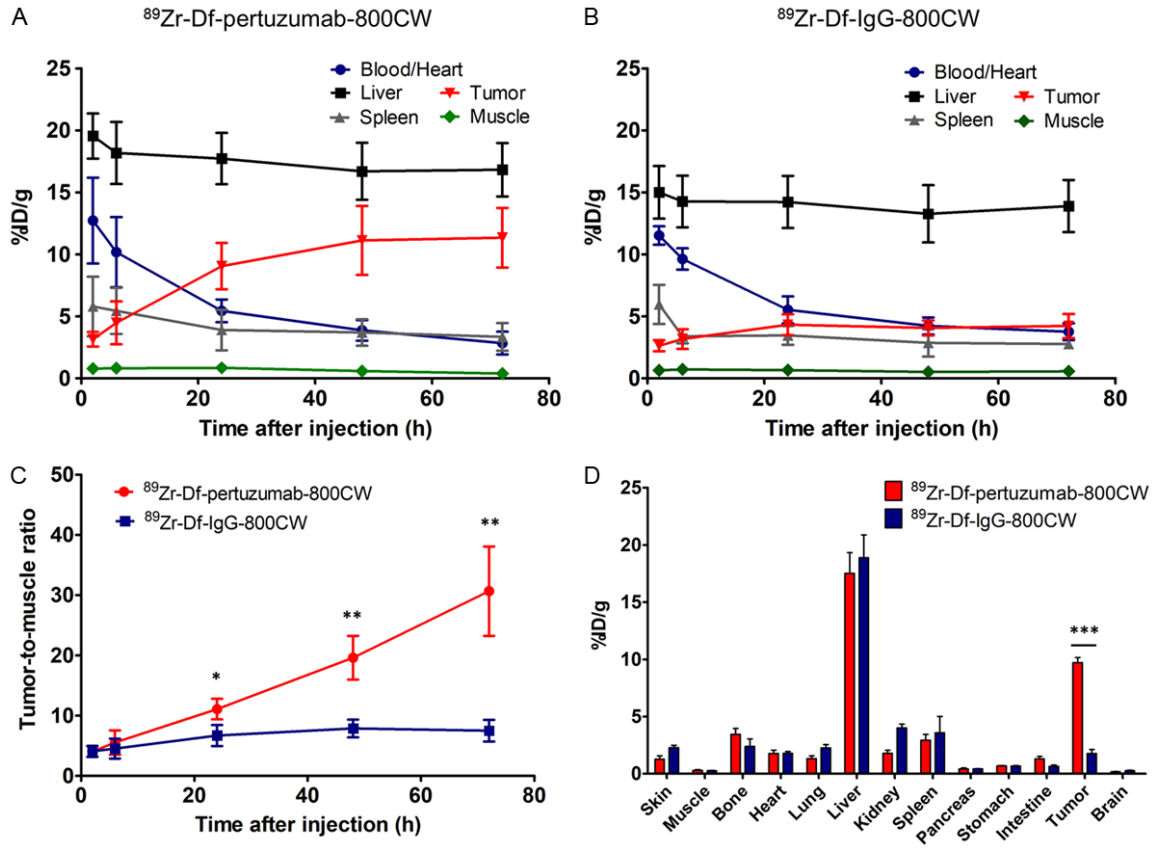

Figure 3. Quantitative region-of-interest analysis of PET imaging over time and *ex vivo* biodistribution results at 72 h after injection of the tracers. Time-activity curves after administration of (A) ^{89}Zr-Df-pertuzumab-800CW and (B) ^{89}Zr-Df-IgG-800CW in subcutaneous SKOV3 tumor-bearing mice. (C) The tumor-to-muscle ratio was significantly higher in the ^{89}Zr-Df-pertuzumab-800CW group than in the ^{89}Zr-Df-IgG-800CW group after 24 h (*P < 0.05, **P < 0.01; n = 3-4). (D) *Ex vivo* biodistribution results also confirmed that tumor uptake of ^{89}Zr-Df-pertuzumab-800CW was significantly higher than that of the control IgG group (***P < 0.001).

Fluobeam instrument allowed tumor resection to be performed with almost real-time image guidance by providing visualization of fluorescence signal. Use of this instrument revealed remaining fluorescence signal sensitively after initial gross tumor surgical removal, leading to a second round of surgical removal in some of the mice (Figure S1). In addition, intraoperative imaging using the Fluobeam demonstrated higher imaging contrast than was observed with post-operative images from other instruments (Figure S1). Postoperative images from the NIRF and CL imaging confirmed that no notable fluorescence or Cerenkov signal was left in the region of the tumor after final tumor resection (**Figure 4B** and **4C**). Additionally, HARLI images indicated that the detected β particles markedly decreased to a background level after tumor removal, and detected counts from the tumors were similar both *in vivo* before surgery and *ex vivo* after tissue resection (**Figure 4D**).

Ex vivo NIRF and CL imaging results indicated that the highest signal from ^{89}Zr-Df-pertuzumab-800CW was in the tumor (**Figure 4B** and **4C**). In addition, the biodistribution results confirmed a statistically significant difference between ^{89}Zr-Df-pertuzumab-800CW and ^{89}Zr-Df-IgG-800CW in tumor uptake (9.7 ± 0.9 vs. 1.8 ± 0.6 %ID/g, P < 0.001, n = 3-4) as well as in tumor-to-muscle ratio (38.7 ± 18.0 vs. 6.6 ± 1.1, P < 0.05, n = 3-4), which correlates with the *in vivo* PET imaging results (**Figure 3D**).

Serial PET/NIRF imaging and image-guided tumor resection in orthotopic tumor models

The presence of orthotopic tumors was confirmed by ultrasonography 3-4 weeks after

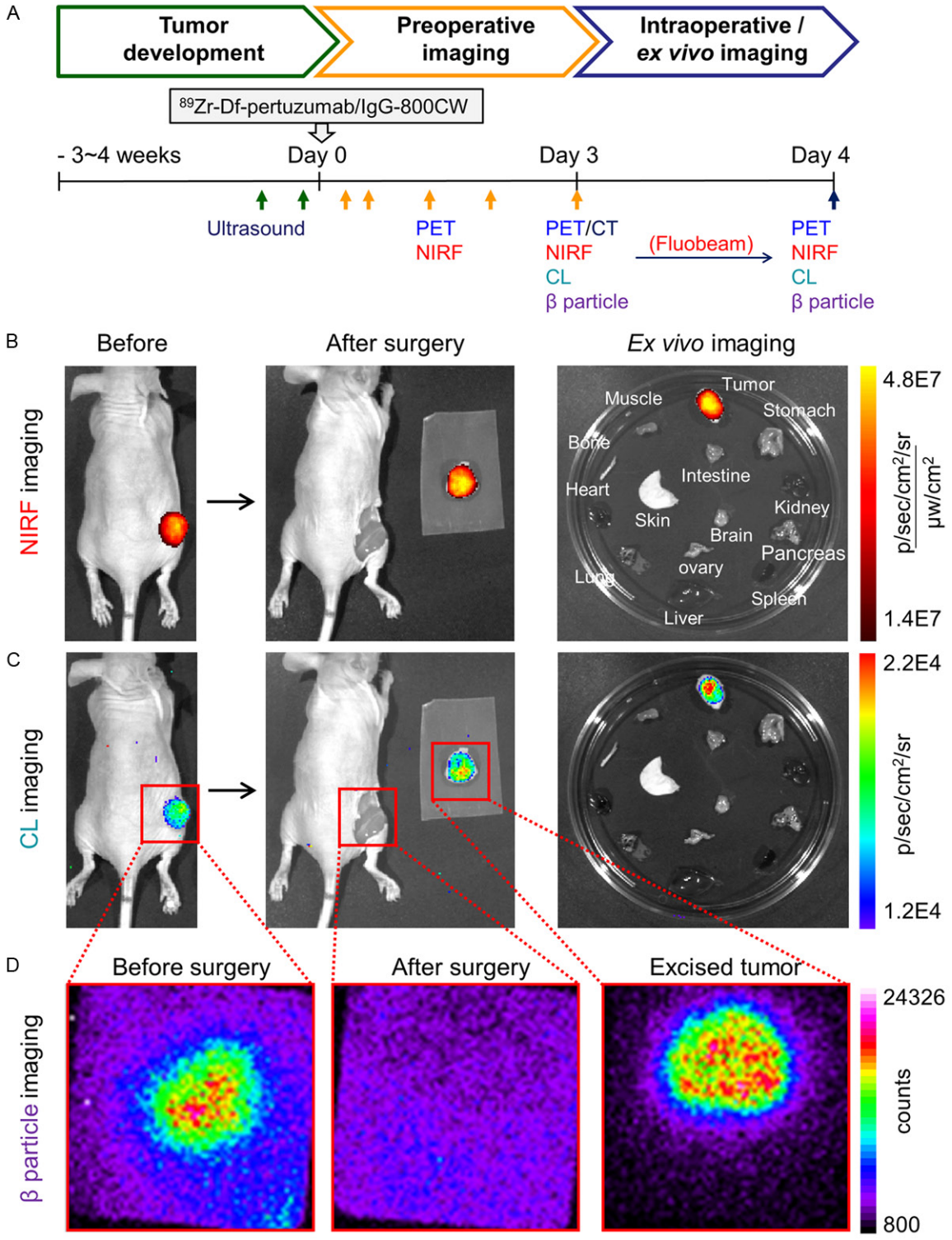

Figure 4. Image-guided tumor resection in the subcutaneous SKOV3 tumor model after the last time point (72 h) of serial PET/NIRF imaging. The same mouse shown in **Figure 2A** is here presented in **Figure 4**. (A) Schematic diagram of using multimodalities for verification of tumor development, preoperative and intraoperative/*ex vivo* imaging. The length of the scale does not reflect actual time. (B-D) Image-guided surgery with (B) Fluorescence-based imaging, (C) Cerenkov luminescence (CL) imaging, and (D) β particle imaging. Red boxes are the expected field of view during HARLI imaging. The actual field-of-view was 2.17 × 2.17 cm^2.

tumor implantation (Figure S2). Even though the tumor cells were injected into the ovary, tumor masses were also observed adjacent to the ovary. The sizes of orthotopic tumors ranged from 1-5 mm in diameter.

Similar to imaging of subcutaneous tumors, serial PET and NIRF imaging with ^{89}Zr-Df-pertuzumab-800CW were performed for the orthotopic SKOV3 tumor-bearing mice (Figure S3). In addition to ultrasonography, PET/CT images at 72 h after injection of the tracers also confirmed the presence of orthotopic ovarian tumors (**Figure 5A**). The tumor uptake of the tracer in the orthotopic models peaked at 48 h (13.2 ± 2.2 %ID/g) and slightly reduced at 72 h (12.3 ± 1.1 %ID/g).

Image-guided orthotopic tumor resection was executed in a similar manner as for the subcutaneous tumor models. During surgery, orthotopic tumors were outlined and removed based on the preoperative NIRF, CL, and β particle imaging (**Figure 5C-E**). In some of the mice, non-target signals such as fluorescence from food in the stomach and accumulation of free ^{89}Zr in the bones were also observed with NIRF and CL imaging, respectively (**Figure 5F**). Furthermore, Fluobeam images allowed detection of tumor tissues along the fallopian tubes (Figure S4). Notably, in HARLI imaging, β particle counts remaining in the abdomen near the removed tissue were higher than expected after tumor removal, which could have resulted from relatively wide imaging field-of-view (2.17 × 2.17 cm^2) compared to the size of the mice, meaning that the detector might collect signals from organs near the orthotopic tumors (**Figure 5E**). *Ex vivo* imaging of harvested organs and the biodistribution study confirmed the uptake of the tracer in the orthotopic tumors (Tumor-to-muscle ratio: 22.2 ± 11.5; n = 5, **Figure 6A** and **6B**). In addition, hematoxylin and eosin staining also verified the malignancy of excised tumor/ovary tissues (**Figure 6C**).

Immunofluorescence staining

Positive staining of HER2 was pronounced in tumor sections acquired from both subcutaneous and orthotopic models. In addition, the results of immunofluorescence imaging in normal ovaries verified that the *in vivo* imaging signals came from human HER2 expression on tumor cells, not from intrinsic expression of HER2 in the ovary, since pertuzumab does not cross-react with the mouse antigen (**Figure 7**). Little signal in organs other than tumor such as the liver suggests that *in vivo* liver uptake is not due to binding of the tracers but likely from the metabolism of the antibodies (Figure S5).

Discussion

Ovarian cancer is one of the widely used models for studies of image-guided surgery. In previous studies, molecular probes including fluorophore-conjugated galactosyl serum albumin [19], avidin [20], and folic acids [21] were used for targeting ovarian cancer. Using peptides or analogues of ligands as imaging agents usually requires a short time to reach notable tumor-to-background contrast but can show high false positive rates if they are non-targeted probes [5]. On the other hand, bevacizumab or trastuzumab-based probes have allowed tumor detection with high specificity during intraoperative NIRF imaging [11]. In addition, Holland et al. used ^{89}Zr-DFO-trastuzumab for CL image-guided surgery of HER2-expressing cancers [22]. In this regard, the present study of dual-labeled pertuzumab examined four different modalities (PET/CT, NIRF, CL, and β particle imaging) for ovarian cancer imaging and may suggest effective combinations for image-guided surgery.

Flow cytometry results confirmed high expression of HER2 on SKOV3 cells (**Figure 1**). Furthermore, serial PET and NIRF imaging with ^{89}Zr-Df-pertuzumab-800CW clearly visualized both subcutaneous and orthotopic ovarian tumors (**Figures 2** and S3). In particular, PET imaging results showed that ^{89}Zr-Df-pertuzumab-800CW specifically accumulated in tumors, while ^{89}Zr-Df-IgG-800CW remained at background levels (Tumor-to-muscle ratio: 30.7± 7.4 vs. 7.5 ± 1.8, P < 0.01, n = 3-4; **Figure 3C**). The significant difference between ^{89}Zr-Df-pertuzumab-800CW and the control group appeared as early as 24 h p.i. in the subcutaneous model. Therefore, ^{89}Zr-Df-pertuzumab-800CW showed promising *in vitro* and preoperative imaging results, indicating the potential of the same probe for image-guided surgery in ovarian cancer.

Some interesting phenomena were observed during *in vivo* imaging. First, in the PET/CT imaging, tumor accumulation in the orthotopic

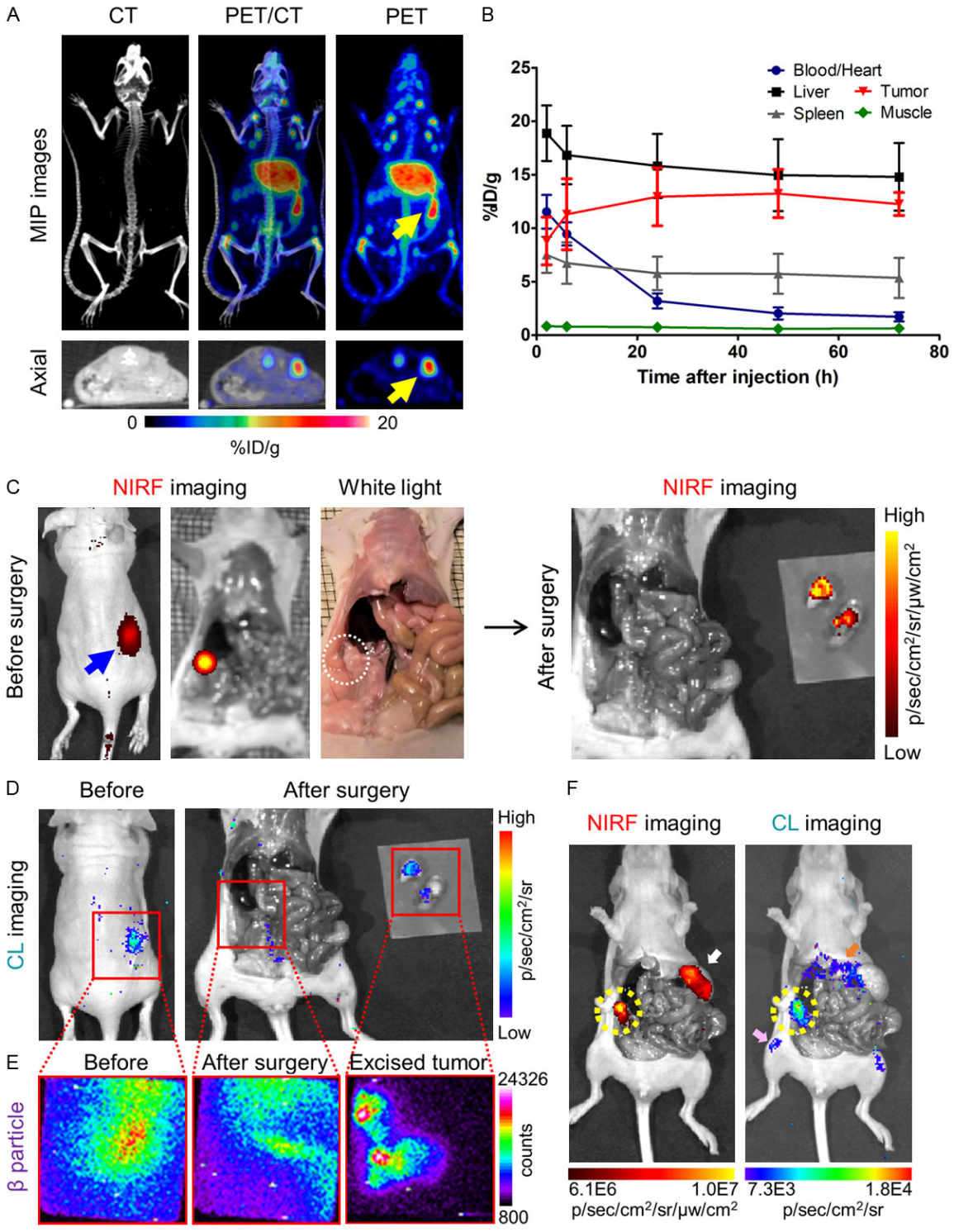

Figure 5. Preoperative/intraoperative imaging and quantitative analysis in orthotopic SKOV3 tumor-bearing mice. (A) PET/CT maximum intensity projection (MIP) and axial images of orthotopic SKOV3 tumor-bearing mice at 72 h after injection of ^{89}Zr-Df-pertuzumab-800CW. The yellow arrows indicate the location of the tumors. (B) Time-activity curve based on PET imaging of orthotopic SKOV3 tumor models after intravenous injection of ^{89}Zr-Df-pertuzumab-800CW (n = 5). The mean tumor uptake (%ID/g) peaked at 48 h after injection of the tracer. (C) Preoperative near-infrared fluorescence (NIRF) imaging at 72 h post-injection of the tracer and image-guided surgery based on white light and NIRF imaging. Both the blue arrow and the white dotted circle indicate the location of the tumor. (D, E) Image guided surgery with (D) Cerenkov luminescence (CL) and (E) β particle imaging. Red boxes are the expected field

of view during β particle imaging. The actual field-of-view was 2.17 × 2.17 cm^2. (F) Examples of non-target signals detected by NIRF and CL imaging in the orthotopic model. The yellow-dotted circle indicates the SKOV3 orthotopic tumors, while white, pink, and orange arrows represent the stomach, bone, and liver of the SKOV3 tumor-bearing mice, respectively.

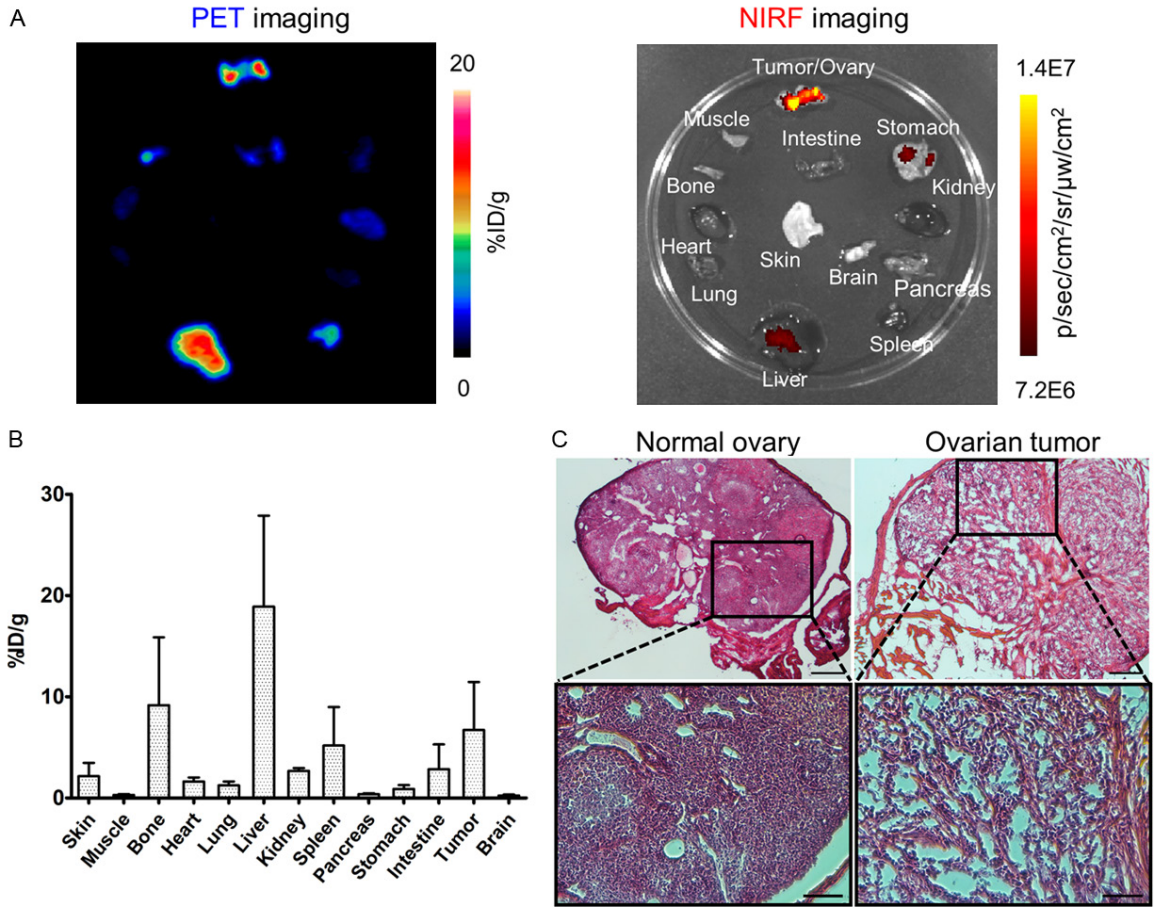

Figure 6. Ex *vivo* imaging and a biodistribution study of ^{89}Zr-Df-pertuzumab-800CW in orthotopic SKOV3 tumor-bearing mice were performed for confirmation of results of preoperative and intraoperative imaging. (A) *Ex vivo* PET images and near-infrared fluorescence images of the organs collected from the mouse in **Figure 5A-E**. (B) Biodistribution of ^{89}Zr-Df-pertuzumab-800CW in orthotopic SKOV3 tumor-bearing mice at 72 h post-injection of the tracer (n = 5). (C) Hematoxylin and eosin staining of normal ovary and excised ovarian tumor sections during surgery. The scale bars are 250 μm and 100 μm for low and high magnifications, respectively.

model was higher than that in the subcutaneous model at early time points (2 h: 8.8 ± 2.2 vs. 3.2 ± 0.6 %ID/g, $P < 0.01$; 6 h: 11.3 ± 3.3 vs. 4.5 ± 1.7 %ID/g, $P < 0.05$, n = 4-5; **Figures 3A** and **5B**), which may be partly explained by the high vascularization of orthotopic tumors [23]. However, after 72 h p.i., the *ex vivo* biodistribution study showed less accumulation of the tracer in orthotopic tumors than expected, which may have resulted from an increase in the removed tissue mass because of normal tissues from margins being resected together with tumor tissues during surgery (**Figure 6B**). In addition, while $^{89}Zr^{4+}$ is trapped after internalization into cells and contributes to sustained PET signals, dyes will often lose their fluorescence properties over time as a result of their degradation. These phenomena are shown in the serial PET and NIRF imaging, wherein PET signals increased in the tumors over time, while NIRF did not exhibited the same trend and may thus have not reflected the actual concentration of pertuzumab in the tumors (**Figures 2** and S3) [24].

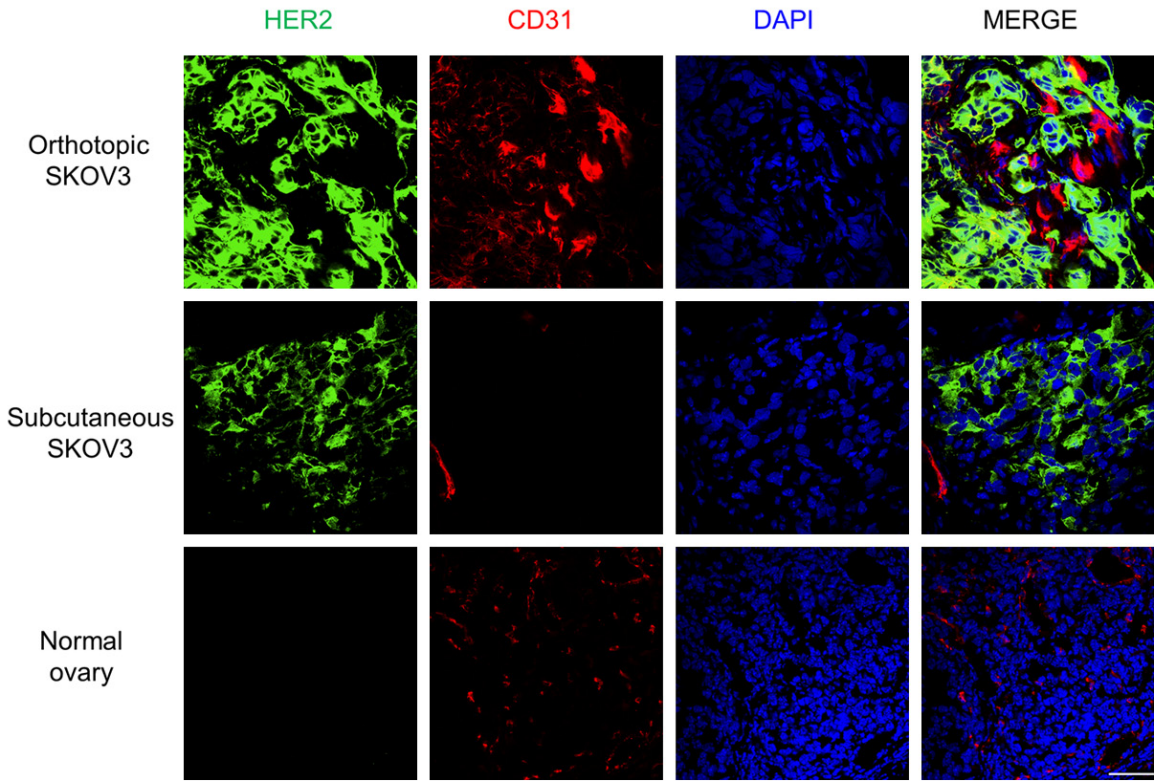

Figure 7. Immunofluorescent staining of orthotopic and subcutaneous SKOV3 tumors and a normal mouse ovary. Human HER2 signal is presented in green, and CD31 (red) and DAPI (blue) staining visualize the locations of vasculature and cell nuclei, respectively. Green signal was pronounced in both orthotopic and subcutaneous SKOV3, while it was undetectable in normal ovaries. Scale bar = 50 μm. (For images of other organs [liver, spleen, and kidney], the reader is referred to the supporting information).

In vivo imaging and biodistribution studies herein showed relatively low tumor accumulation and enhanced liver uptake compared to previous studies using ^{89}Zr-labeled pertuzumab [25] or other dual-labeled mAbs [26]. Our flow cytometry studies showed that conjugation of Df and IRDye 800CW did not impair the specificity or affinity of the tracers for their target (**Figure 1**). In addition, there is a report that ~4 Df groups and ~1 IRDye 800CW molecule can be conjugated to a single antibody, respectively, without compromising of its in vitro and in vivo characteristics [27]. However, since there is still a chance that chelator or dye conjugation can alter the physical characteristics of an antibody or its intermolecular interactions within the body by inducing changes of conformation, charge density or hydrophobicity in the mAb, further investigation may be needed in this regard [28]. Furthermore, both chelator and dye conjugation shared the amine groups of the antibodies resulting in nonspecific conjugation in this study. Therefore, site-specific conjugation could be considered as a future development to optimize the dual-labeling of mAbs.

In this study, we examined the possibility of using dual-labeled pertuzumab for pre/intraoperative imaging with various imaging modalities. Each modality has its own advantages and disadvantages, so researchers and clinicians may be able to choose the proper combination of these modalities depending on their purpose and the availability of the equipment. Based on our study results, we envision a number of possible clinical scenarios. First, for preoperative imaging of ovarian cancer, ultrasonography can be employed as a screening test to look at the uterus, fallopian tubes, as well as ovaries and to find abnormal masses in the ovaries [29]. PET/CT may also play an important role, if suspicious lesions are found, since it allows functional and molecular imaging and quantification of tracer uptake with unlimited tissue penetration, providing information on the location and extent of tumor burden.

Next, for intraoperative imaging, fluorescence, CL, and β particle imaging using hand-held devices can be considered. The use of a fluorescence imaging system using a NIR fluorophore may be the first choice since it is relatively inexpensive and can detect tumor tissues in a sensitive manner without the risk of radiation exposure. In particular, the Fluobeam system was found useful for complete removal of fluorescently-labeled tissues in our study. However, reduced fluorescence signal was observed at the later time points and autofluorescence was also detected in organs other than tumor tissues (**Figures 5F** and S3). On the other hand, CL imaging was free of autofluorescence or reflection from the excitation light since it did not require an external excitation source. Instead, CL imaging showed signals from bones where free radionuclide (^{89}Zr) can accumulate, pointing to the importance of double-checking imaging signals with multiple imaging modalities to piece apart true and false positives (**Figure 5F**). Similar to PET imaging, CL imaging could also visualize the uptake of radiotracers with high sensitivity, but risks from radiation exposure to patients and clinicians still remain. The hand-held charged-particle detector, HARLI, has a relatively high spatial resolution of 42 μm as compared to PET with approximately 1-2 mm and 4-6 mm resolution for preclinical and clinical instruments, respectively [30]. Also, the relatively short exposure time (30 sec) of HARLI data acquisition compared to CL imaging (1-5 min) was another merit of using this hand-held device in our study [13]. However, as shown in our experiment, when the field-of-view for imaging is too wide for the subjects, accurate detection of small tumors can be hampered due to signals from other organs. Nonetheless, if this instrument is applied to patients or large animals, the problem of signal interference from other organs with high accumulation of the tracers may be mitigated. Furthermore, a standard camera providing white-light images can also be used as an adjunct with these various modalities to obtain anatomical as well as functional information.

Taken together, pertuzumab conjugated with ^{89}Zr and IRDye 800CW allowed the detection and removal of ovarian tumors in both subcutaneous and orthotopic models. Since ovarian cancer is vulnerable to peritoneal metastasis, this tracer may also find potential in metastatic ovarian cancer models or other cancers overexpressing HER2. In addition, improvement of the dual-labeled mAbs with different radionuclides or fluorophores may further optimize its clinical potential.

Conclusion

In this study, we demonstrated that pertuzumab conjugated with ^{89}Zr and IRDye 800CW could be employed for pre-, and intraoperative imaging of HER2+ cancer in an effective manner. In this regard, development of dual-labeled mAbs conjugated with a radionuclide with a long-half life and a NIR fluorophore may hold promise for diagnosis, staging, image-guided surgery, and even post-operative care in the clinical setting, leading to improved patient outcomes in the future.

Acknowledgements

This work was supported, in part, by the University of Wisconsin-Madison, the National Institutes of Health (P30CA014520, T32GM0085-05, T32CA009206), and the Brazilian Science Without Borders Program (No. SwB-CNPq). We also would like to acknowledge scientific support from Lightpoint Medical and the Small Animal Imaging and Radiotherapy Facility (SAIRF) at the University of Wisconsin-Madison.

Disclosure of conflict of interest

None.

Address correspondence to: Dr. Weibo Cai, Departments of Radiology and Medical Physics, University of Wisconsin-Madison, Wisconsin, USA. Tel: 608-262-1749; E-mail: wcai@uwhealth.org

References

[1] Sharma SK, Nemieboka B, Sala E, Lewis JS and Zeglis BM. Molecular imaging of ovarian cancer. J Nucl Med 2016; 57: 827-833.
[2] Siegel RL, Miller KD and Jemal A. Cancer statistics, 2019. CA Cancer J Clin 2019; 69: 7-34.
[3] Stewart C, Ralyea C and Lockwood S. Ovarian cancer: an integrated review. Semin Oncol Nurs 2019; 35: 151-156.
[4] Dochez V, Caillon H, Vaucel E, Dimet J, Winer N and Ducarme G. Biomarkers and algorithms for diagnosis of ovarian cancer: CA125, HE4,

RMI and ROMA, a review. J Ovarian Res 2019; 12: 28.
[5] Hekman MCH, Boerman OC, Bos DL, Massuger LFAG, Weil S, Grasso L, Rybinski KA, Oosterwijk E, Mulders PFA, Rijpkema M. Improved intraoperative detection of ovarian cancer by folate receptor alpha targeted dual-modality imaging. Mol Pharm 2017; 14: 3457-3463.
[6] Lim MC, Seo SS, Kang S, Kim SK, Kim SH, Yoo CW and Park SY. Intraoperative image-guided surgery for ovarian cancer. Quant Imaging Med Surg 2012; 2: 114-117.
[7] Ataseven B, Grimm C, Harter P, Heitz F, Traut A, Prader S and du Bois A. Prognostic impact of debulking surgery and residual tumor in patients with epithelial ovarian cancer FIGO stage IV. Gynecol Oncol 2016; 140: 215-220.
[8] Belhocine T, Spaepen K, Dusart M, Castaigne C, Muylle K, Bourgeois P, Bourgeois D, Dierickx L and Flamen P. 18FDG PET in oncology: the best and the worst (Review). Int J Oncol 2006; 28: 1249-1261.
[9] Richard SD, Bencherif B, Edwards RP, Elishaev E, Krivak TC, Mountz JM and DeLoia JA. Noninvasive assessment of cell proliferation in ovarian cancer using [18F] 3'deoxy-3-fluorothymidine positron emission tomography/computed tomography imaging. Nucl Med Biol 2011; 38: 485-491.
[10] Keereweer S, Van Driel PB, Snoeks TJ, Kerrebijn JD, Baatenburg de Jong RJ, Vahrmeijer AL, Sterenborg HJ and Lowik CW. Optical image-guided cancer surgery: challenges and limitations. Clin Cancer Res 2013; 19: 3745-3754.
[11] Terwisscha van Scheltinga AG, van Dam GM, Nagengast WB, Ntziachristos V, Hollema H, Herek JL, Schroder CP, Kosterink JG, Lub-de Hoog MN and de Vries EG. Intraoperative near-infrared fluorescence tumor imaging with vascular endothelial growth factor and human epidermal growth factor receptor 2 targeting antibodies. J Nucl Med 2011; 52: 1778-1785.
[12] Zhao J, Chen J, Ma S, Liu Q, Huang L, Chen X, Lou K and Wang W. Recent developments in multimodality fluorescence imaging probes. Acta Pharm Sin B 2018; 8: 320-338.
[13] Grootendorst MR, Cariati M, Kothari A, Tuch DS and Purushotham A. Cerenkov luminescence imaging (CLI) for image-guided cancer surgery. Clin Transl Imaging 2016; 4: 353-366.
[14] Franklin MC, Carey KD, Vajdos FF, Leahy DJ, de Vos AM and Sliwkowski MX. Insights into ErbB signaling from the structure of the ErbB2-pertuzumab complex. Cancer Cell 2004; 5: 317-328.
[15] Jiang D, Im HJ, Sun H, Valdovinos HF, England CG, Ehlerding EB, Nickles RJ, Lee DS, Cho SY, Huang P and Cai W. Radiolabeled pertuzumab for imaging of human epidermal growth factor receptor 2 expression in ovarian cancer. Eur J Nucl Med Mol Imaging 2017; 44: 1296-1305.
[16] Lam K, Chan C and Reilly RM. Development and preclinical studies of (64) Cu-NOTA-pertuzumab F (ab') 2 for imaging changes in tumor HER2 expression associated with response to trastuzumab by PET/CT. MAbs 2017; 9: 154-164.
[17] Hong H, Zhang Y, Severin GW, Yang Y, Engle JW, Niu G, Nickles RJ, Chen X, Leigh BR, Barnhart TE and Cai W. Multimodality imaging of breast cancer experimental lung metastasis with bioluminescence and a monoclonal antibody dual-labeled with 89Zr and IRDye 800CW. Mol Pharm 2012; 9: 2339-2349.
[18] Holland JP, Divilov V, Bander NH, Smith-Jones PM, Larson SM and Lewis JS. 89Zr-DFO-J591 for immunoPET of prostate-specific membrane antigen expression in vivo. J Nucl Med 2010; 51: 1293-1300.
[19] Gunn AJ, Hama Y, Koyama Y, Kohn EC, Choyke PL and Kobayashi H. Targeted optical fluorescence imaging of human ovarian adenocarcinoma using a galactosyl serum albumin-conjugated fluorophore. Cancer Sci 2007; 98: 1727-1733.
[20] Hama Y, Urano Y, Koyama Y, Kamiya M, Bernardo M, Paik RS, Krishna MC, Choyke PL and Kobayashi H. In vivo spectral fluorescence imaging of submillimeter peritoneal cancer implants using a lectin-targeted optical agent. Neoplasia 2006; 8: 607-612.
[21] van Dam GM, Themelis G, Crane LM, Harlaar NJ, Pleijhuis RG, Kelder W, Sarantopoulos A, de Jong JS, Arts HJ, van der Zee AG, Bart J, Low PS and Ntziachristos V. Intraoperative tumor-specific fluorescence imaging in ovarian cancer by folate receptor-alpha targeting: first in-human results. Nat Med 2011; 17: 1315-1319.
[22] Holland JP, Normand G, Ruggiero A, Lewis JS and Grimm J. Intraoperative imaging of positron emission tomographic radiotracers using Cerenkov luminescence emissions. Mol Imaging 2011; 10: 177-186, 171-173.
[23] Zhang Y, Toneri M, Ma H, Yang Z, Bouvet M, Goto Y, Seki N and Hoffman RM. Real-time GFP intravital imaging of the differences in cellular and angiogenic behavior of subcutaneous and orthotopic nude-mouse models of human PC-3 prostate cancer. J Cell Biochem 2016; 117: 2546-2551.
[24] Hernandez R, Sun H, England CG, Valdovinos HF, Ehlerding EB, Barnhart TE, Yang Y and Cai W. CD146-targeted immunoPET and NIRF imaging of hepatocellular carcinoma with a dual-labeled monoclonal antibody. Theranostics 2016; 6: 1918-1933.

[25] Marquez BV, Ikotun OF, Zheleznyak A, Wright B, Hari-Raj A, Pierce RA and Lapi SE. Evaluation of (89) Zr-pertuzumab in breast cancer xenografts. Mol Pharm 2014; 11: 3988-3995.
[26] Zhang Y, Hong H, Severin GW, Engle JW, Yang Y, Goel S, Nathanson AJ, Liu G, Nickles RJ, Leigh BR, Barnhart TE and Cai W. ImmunoPET and near-infrared fluorescence imaging of CD105 expression using a monoclonal antibody dual-labeled with (89) Zr and IRDye 800CW. Am J Transl Res 2012; 4: 333-346.
[27] Cohen R, Stammes MA, de Roos IH, Stigter-van Walsum M, Visser GW and van Dongen GA. Inert coupling of IRDye800CW to monoclonal antibodies for clinical optical imaging of tumor targets. EJNMMI Res 2011; 1: 31.
[28] Boswell CA, Tesar DB, Mukhyala K, Theil FP, Fielder PJ and Khawli LA. Effects of charge on antibody tissue distribution and pharmacokinetics. Bioconjug Chem 2010; 21: 2153-2163.
[29] van Nagell JR Jr, Hoff JT. Transvaginal ultrasonography in ovarian cancer screening: current perspectives. Int J Womens Health 2013; 6: 25-33.
[30] Khalil MM, Tremoleda JL, Bayomy TB and Gsell W. Molecular SPECT imaging: an overview. Int J Mol Imaging 2011; 2011: 796025.

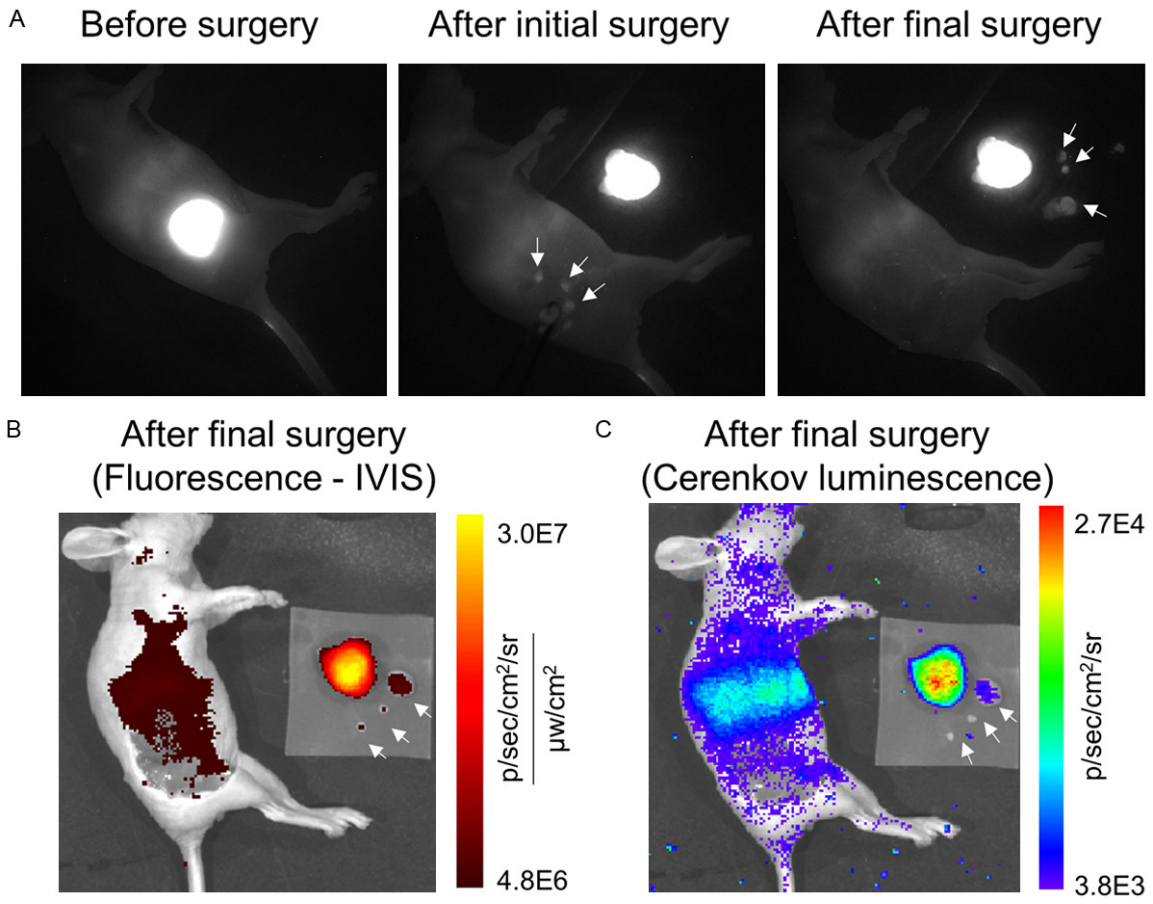

Figure S1. (A) Fluobeam imaging of a subcutaneous SKOV3 tumor with ^{89}Zr-Df-pertuzumab-800CW during image-guided surgery. After initial surgery, fluorescence signals from the remaining tumor tissues were observed (white arrows) and removed after final surgery. Images were taken at a rate of 2 pictures/sec. (B) Fluorescence imaging from the IVIS Spectrum Imaging System, and (C) Cerenkov luminescence imaging after final surgery.

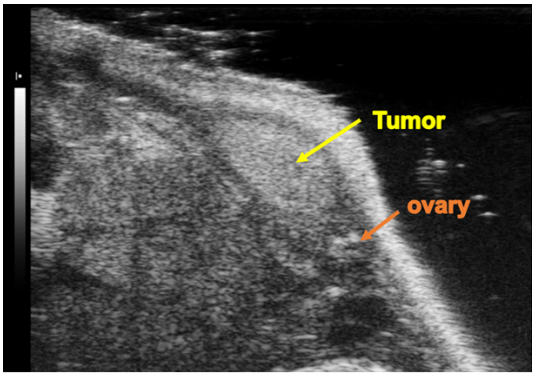

Figure S2. Ultrasound imaging three to four weeks after implantation of SKOV3 tumor cells to validate the orthotopic tumor model. A 40-MHz linear array transducer was utilized for imaging of tumor tissues and ovaries.

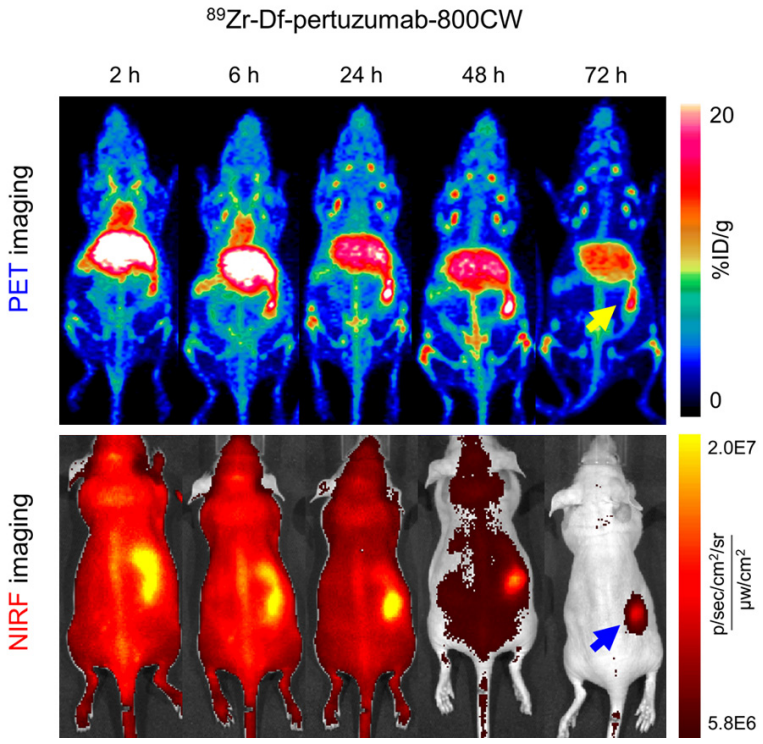

Figure S3. Longitudinal PET and NIRF imaging of the orthotopic ovarian tumor model after injection of ^{89}Zr-Df-pertuzumab-800CW (n = 5). The same mouse shown in **Figure 5A-E** is presented in this figure. Yellow and blue arrows indicate the orthotopic tumor detected from PET and NIRF imaging, respectively.

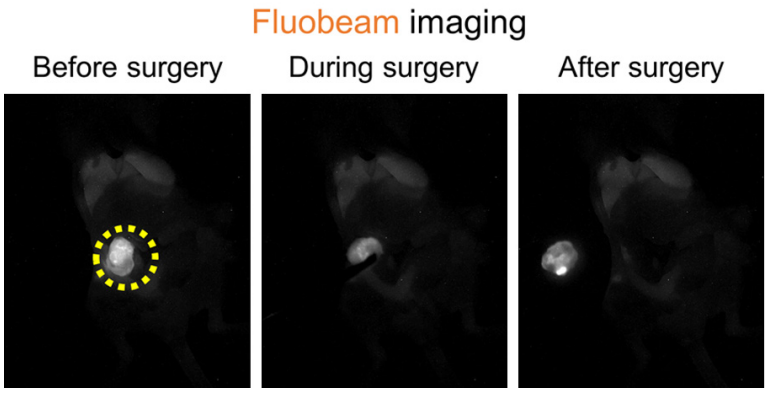

Figure S4. A compilation of images during Fluobeam-guided tumor (yellow-dotted circle) resection of orthotopic ovarian cancer.

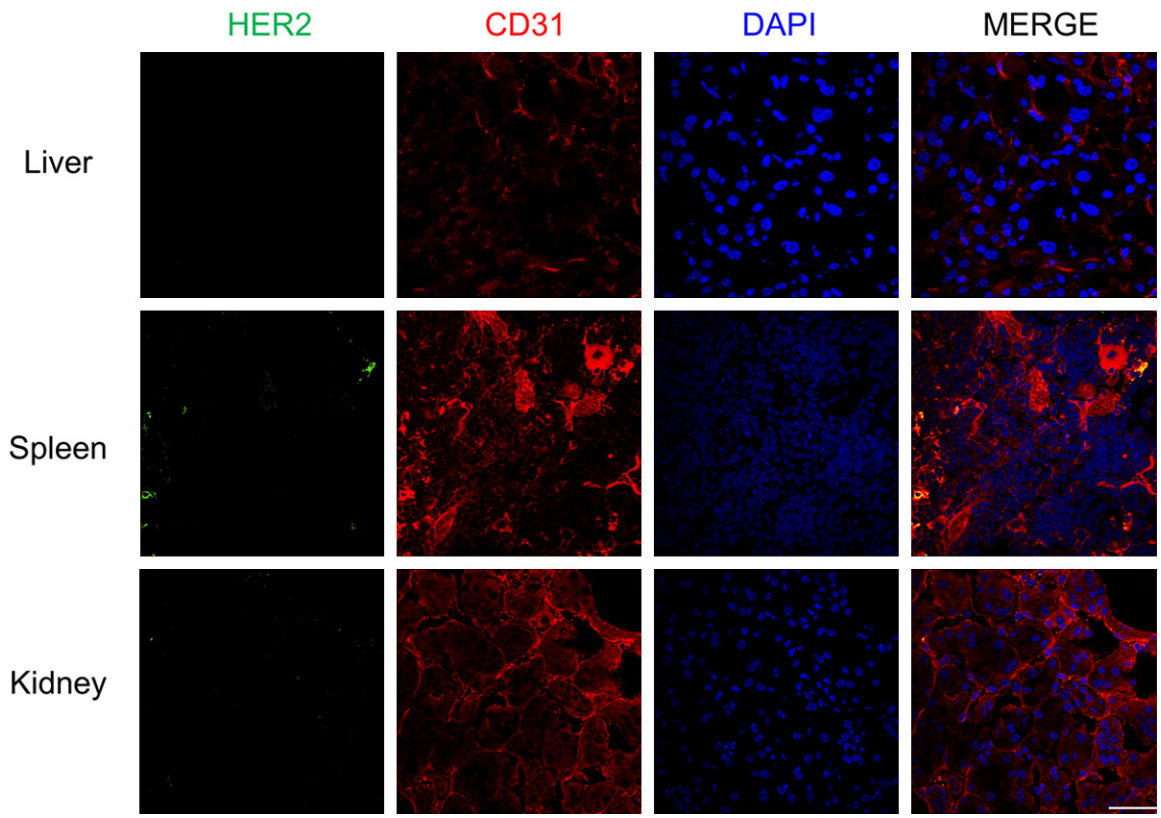

Figure S5. Immunofluorescence staining of liver, spleen and kidney tissues from SKOV3 tumor-bearing mice. Pertuzumab and Alexa Fluor 488 goat anti-human antibodies (green) were used for staining human HER2. CD31 (red) and DAPI (blue) staining indicate the presence of vasculature and cell nuclei, respectively. Scale bar = 50 μm.